



A Versatile Material: Perovskite Bismuth Ferrite Microparticles as a Potential Catalyst for Enhancing Fuel Efficiency and Degradation of Various Organic Dyes

Shanza Rauf Khan¹ · Saba Jamil^{1,4} · Shamsa Bibi¹ · Sarmed Ali² · Tanzila Habib¹ · Muhammad Ramzan Saeed Ashraf Janjua³

Received: 6 February 2020 / Accepted: 24 March 2020 / Published online: 27 March 2020
© Springer Science+Business Media, LLC, part of Springer Nature 2020

Abstract

The investigation of photocatalytic and fuel additive properties of bismuth ferrite (BiFeO_3) microparticles is main objective of this work. Individual properties of bismuth and iron are synergistically reinforce in BiFeO_3 . X-ray diffraction spectroscopy is used to analyze the phase, phase purity and lattice structure of BiFeO_3 . Fuel additive and photocatalytic nature are linked to morphology and size of particles. Morphological analysis showed that rod like particles are arranged in the form of star like structures. Fuel additive role of BiFeO_3 is analyzed by testing calorific value, flash point, fire point, surface tension, kinematic viscosity, cloud point and pour point of fuel loaded with 20, 40, 60 and 80 ppm additive. Amount of additive has affected all the properties of fuel. So additive role of BiFeO_3 is analyzed which helps to decide whether BiFeO_3 can be used as additive on large scale or not. Photocatalytic degradation of dyes is studied in aqueous medium using BiFeO_3 as photocatalyst. Photocatalytic role of BiFeO_3 is analyzed by measuring apparent rate constant (k_{app}), percentage degradation and degradation time of all dyes. k_{app} of dyes is as follows: CV (0.0371 min^{-1}), RB5 (0.0186 min^{-1}), MR (0.0159 min^{-1}), MB (0.0147 min^{-1}), EBT (0.0142 min^{-1}), MX (0.0135 min^{-1}), CR (0.0133 min^{-1}), FG (0.0098 min^{-1}) and SN (0.0088 min^{-1}). Comparison of all these parameters helps to analyze that degradation of dyes is linked to their structure and nature.

Keywords Bimetallic · Nanoparticles · Catalyst · Additive · Fuel

1 Introduction

Synergistic effect of two distinct metals enhanced their individual properties and new enhanced properties are produced. Bimetallic nanoparticles possess variety in composition,

architecture and properties which enable their applications in field of electrochemistry [1, 2], biomedicine [3–5], catalysis [6–11], sensing [12, 13] and optics [14, 15]. These applications depend on the composition, size, shape and surface chemistry of nanoparticles [16]. Bimetallic nanoparticles have been widely used as catalyst in oxidation, reduction or degradation of chemicals for example oxidation of dyes [17], glucose [18], carbon monoxide [19, 20], benzyl alcohol [21], crotyl alcohol [22], methanol [23], toluene [24], dehydrogenation of propane [25] and hydrogenation of nitroarene [26]. Iron (Fe) nanoparticles are highly reactive towards water and oxygen. So its use become limited in last decade. It is also reported that addition of second metal prevented oxidation of Fe atoms in air and also enhanced the adsorption and surface properties. Therefore Fe based bimetallic nanoparticles such as palladium–iron [27], copper–iron [28], nickel–iron [29] and silver–iron [30] have been fabricated to overcome the problems faced by Fe nanoparticles.

Extensive study has been reported to best tune bismuth (Bi) based bimetallic nanoparticles i.e. bismuth–lead [31],

Electronic supplementary material The online version of this article (<https://doi.org/10.1007/s10904-020-01520-x>) contains supplementary material, which is available to authorized users.

✉ Shanza Rauf Khan
shanza.khan@uaf.edu.pk

¹ Department of Chemistry, University of Agriculture, Faisalabad 38000, Pakistan

² Department of Physics, University of Agriculture, Faisalabad 38000, Pakistan

³ Department of Chemistry, King Fahd University of Petroleum and Minerals, Dhahran 31261, Saudi Arabia

⁴ Department of Materials Science and Engineering, Cornell University, Ithaca 14853, USA

bismuth–tin [32], bismuth–tungsten [33] and bismuth–cadmium [34]. Bi is well known for thermoelectric, diamagnetic and environmentally resistant properties. Bi nanoparticles do not react with media but its band gap is greater than that of Fe nanoparticles. Bi hybridized d band is associated with Fe and present just above the fermi level. Thermoelectric power shown predominance of hole carrier and ferroelectricity that lead to cause G-type antiferromagnetism. Therefore properties of Bi are tried to couple with Fe in the form of bismuth ferrite (BiFeO_3).

Numerous studies has been reported on synthesis, doping and applications of BiFeO_3 nanoparticles. Shokrollahi et al. have used co-precipitation method for the synthesis of BiFeO_3 nanoparticles of 30–60 nm size [35]. Chen et al. have reported that BiFeO_3 was synthesized by hydrothermal method with average size around 5 nm [36]. Lone et al. have synthesized BiFeO_3 nanoparticles by reverse micellar approach [37]. Chakraborty et al. have synthesized BiFeO_3 nanoparticles by sol–gel method [38]. Ruby et al. have synthesized BiFeO_3 nanosheets by microwave assisted approach and studied photocatalytic degradation of methyl orange [39]. Ghahfarokhi et al. [40] and Ponraj et al. [41] have doped BiFeO_3 with various atomic percentage of manganese (Mn) to increase its application scope towards photocatalytic systems. Europium doped BiFeO_3 has been also reported but not applied in any field yet [42]. BiFeO_3 has been also used as reinforcement with graphene matrix for its use as electrode material [43]. BiFeO_3 nano/micro particles have been rarely used as catalyst for degradation of dyes. Copper doped ZrO_2 [44], iron doped ZrO_2 [45], barium titanate [46], cobalt [47], nickel [47] and copper sulphide@titania [48] nanoparticles and graphitic carbon nitride–metal composites [49–51] have been used as catalyst for degradation of dyes and hydrogen production. Numerous catalysts have been reported for degradation of dyes but reusability, leakage and high band gap are the major problems associated with those catalysts [52–58]. Bands of Bi and Fe overlap and band gap is reduced. High hole carrier ability of Fe and inert/non-toxic behavior of Bi has diverted attention of researchers towards its used in field of photocatalysis. In this work, BiFeO_3 microparticles are used as catalyst for degradation of variety of pollutants (including azo dyes). This sort of approach has not been developed previously. So that a single catalyst has been designed for degradation of series of azo dyes. In this work, BiFeO_3 microparticles are also used as additive for commercial fuel to increase its application scope.

Mostly additives are used in the form of oils, polymers and micro/nano particles. Very few reports are available in which detailed synthesis, characterization and formation mechanism of additive micro/nano particles have been discussed. Metal oxide [59, 60], mixed metal oxide [61], bimetallic [62] and many other additives have been

reported by our group. On account of the data, Bi and Fe pair has been designed which can show efficient calorific value similar to cerium oxide nanoparticles, Cerium is well known fuel additive, but its cost and toxic nature always limits its use [63]. Therefore BiFeO_3 is used as additive in fuel and fuel parameters like fire point, flash point, calorific value, specific gravity, surface tension and kinematic viscosity have been analyzed.

BiFeO_3 is first time used as fuel additive and catalyst. This research is focusing on the synthesis of BiFeO_3 through micro-emulsion method by using ferric chloride and bismuth chloride precursors. Obtained product is characterized by X-ray diffraction spectroscopy (XRD) and scanning electron microscopy (SEM). BiFeO_3 microparticles is used in applications as fuel additive and catalyst.

2 Experimental

2.1 Materials

Bismuth chloride (BiCl_3), ferric chloride ($\text{FeCl}_3 \cdot 6\text{H}_2\text{O}$), phenyl hydrazine ($\text{C}_6\text{H}_8\text{N}_2$), *n*-hexane (C_6H_{14}), ethanol ($\text{C}_2\text{H}_5\text{OH}$), hydrochloric acid (HCl), sodium borohydride (NaBH_4), sodium hydroxide (NaOH), polyethylene glycol, hydrogen peroxide (H_2O_2) and acetone ($\text{C}_3\text{H}_6\text{O}$) were purchased from Sigma-Aldrich USA. All the chemicals of research grade were used. Diesel-PSO Limited was used as sample fuel. Distilled water was used throughout experimental work. All chemicals were used as it is without any further purification.

2.2 Synthesis of Bismuth Ferrite Bimetallic Microparticles

100 mL *n*-hexane and 20 mL distilled water were mixed and stirred for 1 h at room temperature. 3 mL polyethylene glycol was added into reaction mixture during stirring. After 1 h microemulsion was divided into two parts. 8 g BiCl_3 and 1.6688 g $\text{FeCl}_3 \cdot 6\text{H}_2\text{O}$ were dissolved in one part of microemulsion and stirred for 1 h. 10 mL reducing agent phenyl hydrazine was dissolved in other part of microemulsion and stirred it for 20 min. Both solutions were mixed and stirred for 1.5 h at room temperature to obtain product. Product was washed 4 times with distilled water. Precipitates were collected by centrifugation at 3000 rpm and dried in oven at 60 °C for 24 h. The dried product was ground and subjected to calcination at 600 °C for 6 h in muffle furnace as shown in Fig. S1.

2.3 Study of Photocatalytic Application

BiFeO₃ microparticles were used as catalyst for degradation of Congo red (CR), methylene blue (MB), methylene red (MR), crystal violet (CV), reactive black 5 (RB5), Eriochrome black T (EBT), fast green (FG), murexide (MX), safranin (SN). 3.5 mL of 0.1 mM dye, 0.2 mL H₂O₂ and 10 mg catalyst were added in a cuvette and absorbance at λ_{\max} of dyes was monitored by UV–Vis spectrophotometry. k_{app} was obtained by plotting graph between $\ln A_t/A_0$ and time using formula $\ln \frac{A_t}{A_0} = -k_{\text{app}} \times t$. Here A_0 is absorbance at time zero and A_t is absorbance at different time. Beer-Lambert's law ($A = \epsilon cl$) was used to determine the concentration (c) of reactants from absorbance (A). ϵ is absorption coefficient of solution and l is path length of cuvette.

2.4 Study of Fuel Additive Application

Different parameters like fire point, flash point, calorific value, surface tension and kinematic viscosity were measured of 20, 40, 60 and 80 ppm additive concentration and sonicated for about 5 min before analysis.

2.5 Characterization

XRD pattern of product was obtained by using Jeol JDX-3532 diffractometer. CuK α radiations at 40 kV and 150 mA in 10°–80° 2-theta range were used. Lattice parameters from XRD data was analyzed by MATCH 3.0 software. VESTA software 3.4.0 was used for the structural analysis of unit cell. SEM FEG-250 Quanta (Thermo Fisher Scientific, USA) is available at National Textile Research Center (NTRC) of National Textile University (NTU), Faisalabad, Pakistan. It has been used for morphological imaging of synthesized product. It is equipped with field emission electron gun (FEG). Sample is coated with gold prior analysis using Sputter Coating Machine. Catalytic activity was checked by VIS-1100 UV–Vis spectrophotometer. ASTM-D 93 Cleveland open Cup Tester, Apex Lab Equipment Company, is used for determination of flash point and fire point of fuel samples. 100 mL of fuel sample was poured into the cup of tester and flame is applied to determine the flash point and fire point. Gravity meter ASTM D 1217 is used for measurement of specific gravity of fuel samples. ASTM D 240 Oxygen Bomb Calorimeter is used for determination of calorific value of fuel samples. 1 mL of fuel sample is poured into the tube of the calorimeter and 220 V is applied to burn the copper wire and ignition is produced. Ostwald's viscometer was used to determine dynamic viscosity of fuel samples. 20 mL fuel sample was taken in viscometer and measured time of measurement of flow of sample through capillary tube. Then

kinematic viscosity is determined by dividing the dynamic viscosity with specific gravity. Cloud point of samples was measured by pouring it into a test jar to a level about half fill. A cork or jar lid was used to close the jar and had a test thermometer. The bulb of thermometer was positioned to the bottom of jar. The entire set up was maintained in constant temperature cooling bath. After every 1 °C, the jar was taken out and cloud point is noted when cloudy appearance was observed in the sample. The temperature was noted when the sample did not flow for 5 s while holding in horizontal direction that temperature noted as pour point.

3 Results and Discussion

3.1 XRD

XRD pattern of bimetallic microparticles is shown in Fig. 1. Majority of the peaks are matched with PDF No. 96-154-2194 which indicated that the synthesized product is BiFeO₃. Sharp peaks are present at 2-theta 30.90°, 32.01°, 45.93°, 51.54°, 55.02°, 57.14° and 67.23° with miller indices (110), (113), (215), (119), (306), (316) and (317) respectively. Less intense peaks are present at 2-theta 22.58°, 37.53°, 39.56°, 45.53°, 51.28°, 60.28°, 65.29° and 71.15° with miller indices (104), (211), (108), (200), (102), (220), (314) and (229) respectively. Presence of sharp peaks in XRD pattern indicates that product is highly crystalline. Many peaks are overlapped at 2theta 61.02°, 75.01°, 47.08° and 39.05° which might be due to the instrumental broadening and may be the reason of noise. Detailed summary of lattice parameters, atomic coordinates, density, volume, crystal system, bond lengths and bond angles are given in Table S1. This data is used to construct structural model given in Fig. S2. Unit cell of BiFeO₃ is trigonal with hexagonal axes and having space

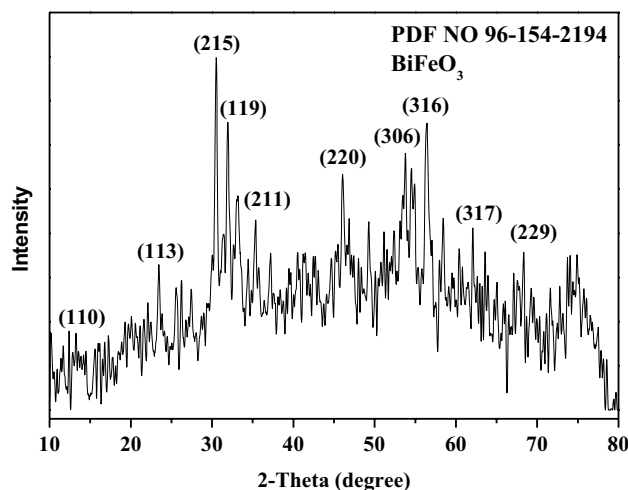


Fig. 1 XRD pattern of BiFeO₃ bimetallic microparticles

group R 3 c (161). The atomic coordinates of Fe, Bi and O are given in Table S1. The structural model indicated the position of Fe, Bi and O atoms in unit cell and their arrangement according to x , y and z axis. Structural model indicates that one Bi atom is surrounded by four Fe atoms and one Fe atom is at center and surrounded by 8 Bi atoms which are located at different positions in unit cell. Trigonal structure of BiFeO_3 is diagrammatically shown in Fig. S2(a). Bi atoms are present in center and corners of unit cell. Every Bi atom is surrounded with six Fe atoms. Bonding between atoms of Fe, Bi and O are shown in Fig. S2(b). Fig. S2(c) explained that Bi atom is surrounded by Fe atoms and formed trigonal structure. Every Bi atom is part of one trigonal but every Fe atom is part of two trigonal connected with each other (Fig. S2(d)). Two planes with miller indices (119) and (316) are shown in Fig. S2(e) and (f) respectively to show the position of atoms. These planes are constructed with their respective d-spacing values obtained from XRD data analysis. The intensity of these planes is maximum among all diffraction peaks, that's why these planes are identified in the structural model. Plane (316) has six atoms with three Bi and three Fe atoms. Plane (119) has only two atoms constituted by one Bi and one Fe atom.

3.2 SEM

SEM images of BiFeO_3 bimetallic microparticles are given in Fig. 2. SEM images are recorded at $\times 6000$ and $\times 8000$ magnifications as shown in Fig. 2a, b respectively. It is observed from images that particles are fused with each other. Few rod like particles are also observed. The dimensions of microrods are almost 5–6 μm and 1.5–2.0 μm . Microrods are arranged in the form of stars. Around five

microrods are joined with each other and formed microstar like assembly. Aggregation of particles is occurred due to high surface energy of particles. So particles fused with each other to decrease their energy. SEM tells about the surface morphology of particles. Size of particles is also calculated from SEM images. Photocatalysis is related to surface of particles. Because adsorption of dyes occurred at surface of catalyst. If particles are non-uniform then distribution of active sites is not uniform and their catalytic activity is affected. The surface area of small particles is greater than that of big particles, so catalytic activity of small particles is found greater than that of big particles.

3.3 Application of FeBiO_3 Microparticles as Fuel Additive

Now a days fuel additives are very demanding therefore microparticles are used as additives to improve the efficiency of fuel. For checking of role of additives, different parameters of diesel are tested. Five samples of different concentration as 0, 20, 40, 60 and 80 ppm are prepared. Different combustion and physical characteristics like flash point, fire point, pour point, cloud point, surface tension, specific gravity and kinematic viscosity are analyzed. Fire and flash points of all samples are tested as a function of different concentrations of additive. Linear decrease in flash and fire points are observed in Fig. 3a. 0 ppm is considered as control because the sample does not contain any additives. Flash point of control sample is measured at 74 $^\circ\text{C}$. The flash point of sample of 20 ppm is 73 $^\circ\text{C}$, 65 $^\circ\text{C}$ for 40 ppm, 64 $^\circ\text{C}$ for 60 ppm and 62 $^\circ\text{C}$ for 80 ppm. Same trend is observed in fire points. Fire points of various samples at 0, 20, 40, 60 and 80 ppm concentration of additives are 82, 81, 71, 70 and

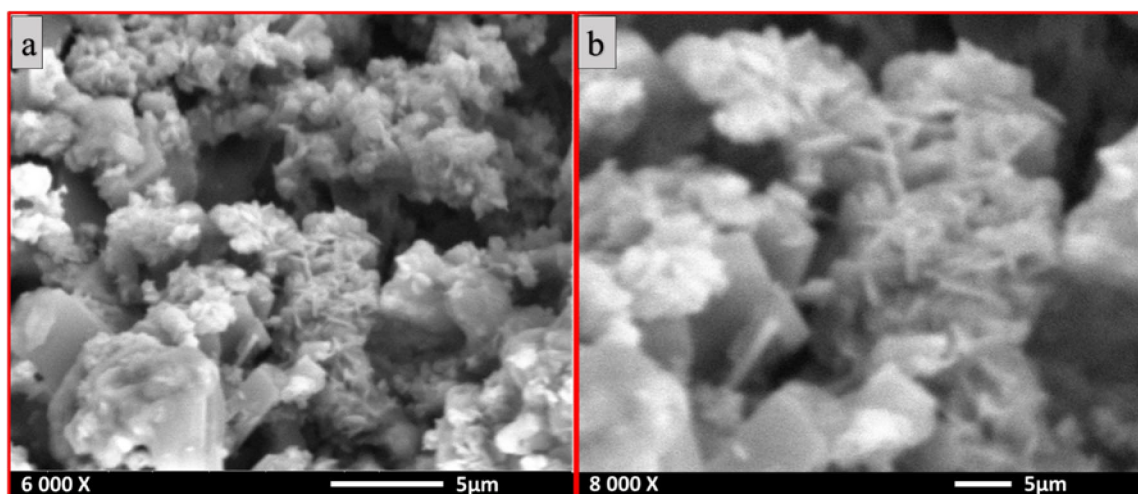
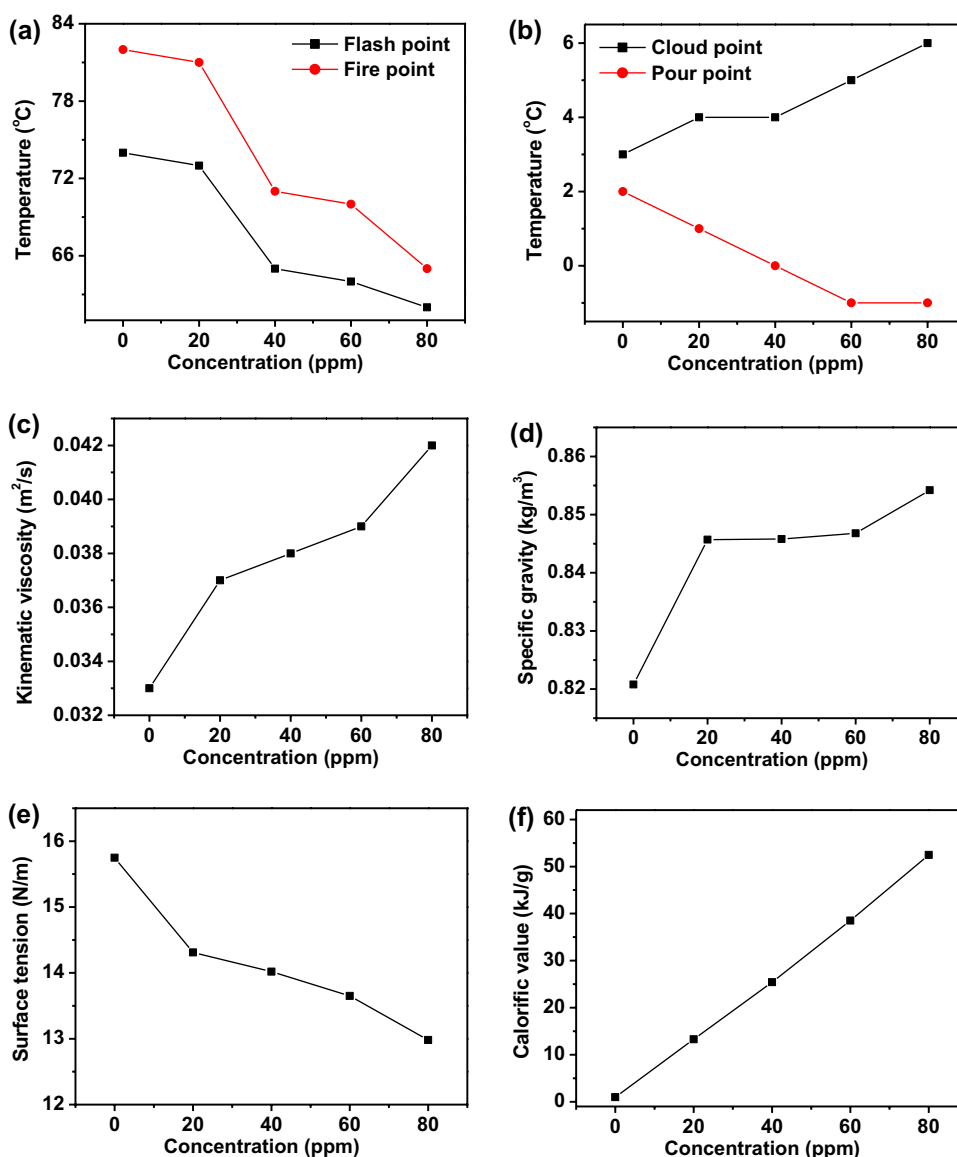


Fig. 2 SEM images of BiFeO_3 microparticles synthesized by microemulsion method **a** overall view and **b** close view of nanorods arranged in the form of stars

Fig. 3 Effect of BiFeO₃ bimetallic microparticles on different parameters of diesel: **a** flash and fire points, **b** cloud and pour points, **c** kinematic viscosity, **d** specific gravity, **e** surface tension, and **f** calorific value



65 °C respectively. Results shows that diesel with different concentrations of additive have lower flash and fire points as compared to control sample. Flash point is the lowest temperature at which fuel start to vaporize and ignite in atmosphere and fire point is the temperature when fuel started to catch fire in the surrounding atmosphere. Vaporization is the property of diesel but it increases after addition of nanoparticles. The attraction forces between the layers are weakened by the addition of nanoparticles that leads to decrease the ignition temperature. These results are in agreement as reported by Zhu et al. and Khan et al.

Cloud and pour points are also tested at different concentrations of additive in diesel and results are given in Fig. 3b. Here non-linear trend is observed in case of cloud point but not in case of pour points. Cloud point is decreased from 4 to 3 °C with increase in concentration

of additives from control to 20 ppm. But cloud point is increased from 4 and 6 °C with further increase in additive from 20 to 80 ppm. The decreasing trend is observed for pour point from 2 to 1 °C for additive dosage from 0 to 20 ppm. The increase in concentration of additive leads to decrease in pour point. The pour point is – 1 °C for sample 60 and 80 ppm both which shows that pour point values are not significantly affected by increasing additive concentration. The results show that diesel crystallization is affected by addition of BiFeO₃ microparticles that suppressed the clouding at 20 ppm. The microparticles provides surface for the adsorption of fuel and fast clouding shows that crystallization of fuel is increased as the concentration of additive is increased. The decreasing trend in pour point is shown to prevent the engine from heating and cause difficulty for diesel to freeze in pipes because during

crystallization microparticles are present and reduce the chance of water that participate in freezing.

The effect of concentration of additive on kinematic viscosity is given as Fig. 3c. Kinematic viscosity for control diesel sample (0 ppm) is $0.033 \times 10^{-4} \text{ m}^2 \text{ s}^{-1}$. Increasing trend is observed with increase of concentration of additives. Kinematic viscosity of sample 20, 40, 60 and 80 ppm are 0.037×10^{-4} , 0.038×10^{-4} , 0.039×10^{-4} and $0.042 \times 10^{-4} \text{ m}^2 \text{ s}^{-1}$ respectively. The result shown that increasing trend in viscosity is decreased the consumption of diesel and make less wear because as the viscosity increase sliding of layers become faster and overlapped on other that cause resistance. Viscous diesel is less combustible and smoke emission is high. But less kinematic viscosity is decreased the turbulent flow of diesel. So the amount of additives should be according to comparison of these facts. Previous work reported by Sajith et al. supported this work [64]. It has been reported that density and kinematic viscosity of nanoemulsion fuels is increased marginally probably due to the presence of water.

Plot of specific gravity of control and modified diesel is given as Fig. 3d. The specific gravity of control is lower than that of modified diesel. It is observed that specific gravity of diesel is increased with increase of additive concentration. The specific gravity values are increased from 0.820 and 0.845 kg/m^3 for additive dosage from 0 to 20 ppm. With the increase of additive dosage as 40, 60 and 80 ppm specific gravity is also increased as 0.845, 0.846 and 0.854 kg/m^3 respectively. Microparticles are of small size with high surface area to volume ratio and diffused between layers of diesel. The empty spaces between layers are filled with nanoparticles and attraction forces become strong and compactness is increased. So density and specific gravity are increased with increase of additive dosage. Khalid et al. have reported the same result [59]. Density is the actual weight of fuel at room temperature and with increase of microparticles it became denser, consequently higher will be specific gravity.

The effect of concentration of additives on surface tension is given in Fig. 3e. It was observed that surface tension of pure diesel is 15.75 N/m. Decreasing trend is observed in the value of surface tension of diesel. Surface tension of diesel decrease from 15.75 to 13.97 N/m with change in additive concentration from 20 to 80 ppm. As the nanoparticles enter into diesel increased particle concentration inside droplet rather than surface and decreased attraction forces at surface. Surface tension of diesel play an important role in the combustion of fuel. Because it effect the initial concentration of fuel combustion such as fuel atomization and spray characteristics. The values of surface tension tends to decrease due to the high solubility of nanoparticles in diesel.

Calorific values is best indicator to check the efficiency of nanoparticles as additives. Increasing trend of calorific

values are given in Fig. 3f. The calorific values are 965, 13,265, 25,410, 38,525 and 52,456 J/g at different concentration of additives as 0, 20, 40, 60 and 80 ppm respectively. It is observed that with the increase of concentration of additives calorific values are also linearly increased. It is due to high surface area of nanoparticles for the absorption of fuel. These nanoparticles are act as catalyst for combustion of fuel because calorific value indicate the combustion characteristics of fuel. As the nanoparticles enter in fuel due to high surface to volume ratio adsorbed large number of diesel on surface of BiFeO_3 microparticles. The literature supported this work [59]. Increase in energy with increase of dosage of additives explore the efficiency of bismuth ferrite bimetallic nanoparticles.

3.4 Application of BiFeO_3 Microparticles as Catalyst for Degradation of Organic Dyes

Catalytic degradation of organic dyes i.e., MR, MB, RB5, CV, CR, FG, EBT, SN and MX is studied and results are shown in Fig. 4a–e. Figure 4a is a plot of $\ln(A_t/A_0)$ versus time for catalytic degradation of MB, MR, CR, CV and RB5. The catalytic degradation of EBT, FG, SN and MX are shown in Fig. 4c. Initially the degradation of dyes was not started that indicated by no change in $\ln(A_t/A_0)$ with passage of time. This period is known as induction period. Diffusion and adsorption of reactants on the surface of microparticles are happened in this duration. The decrease in $\ln(A_t/A_0)$ with time indicates the progress in degradation. Linear region of plot of $\ln(A_t/A_0)$ and time in Fig. 4b, d is used for determination of apparent rate constant (k_{app}). Synergistic effect of Fe and Bi is expressed by the breaking of azo bond in organic dyes by addition of electrons. Transfer of electron hole occurred at catalyst's surface. Conduction band of catalyst contain electrons and H_2O_2 which reacts and produce $\dot{\text{O}}\text{H}^-$ and $\dot{\text{O}}\text{H}$. Oxidization of $\dot{\text{O}}\text{H}^-$ is happened by catalyst surface and transferred electron to conduction band of catalyst along with $\dot{\text{O}}\text{H}$ production. Fast $\dot{\text{O}}\text{H}$ production is occurred by catalyst and holes provided by catalyst. H_2O_2 was also used for the production of hydroxyl group but water solvent may be de-activated the radicals. Both dye and H_2O_2 absorbed on catalyst and reacted with dye before de-activation radicals. Therefore dye degradation become very fast in the presence of catalyst. Different organic dyes shows characteristic peaks in UV–Vis range due to long conjugated pi-system that linked by azo groups [65–68]. Breakage of long conjugated pi-system and degradation of organic dyes are happened by the hydrogenation of azo bond to amino group.

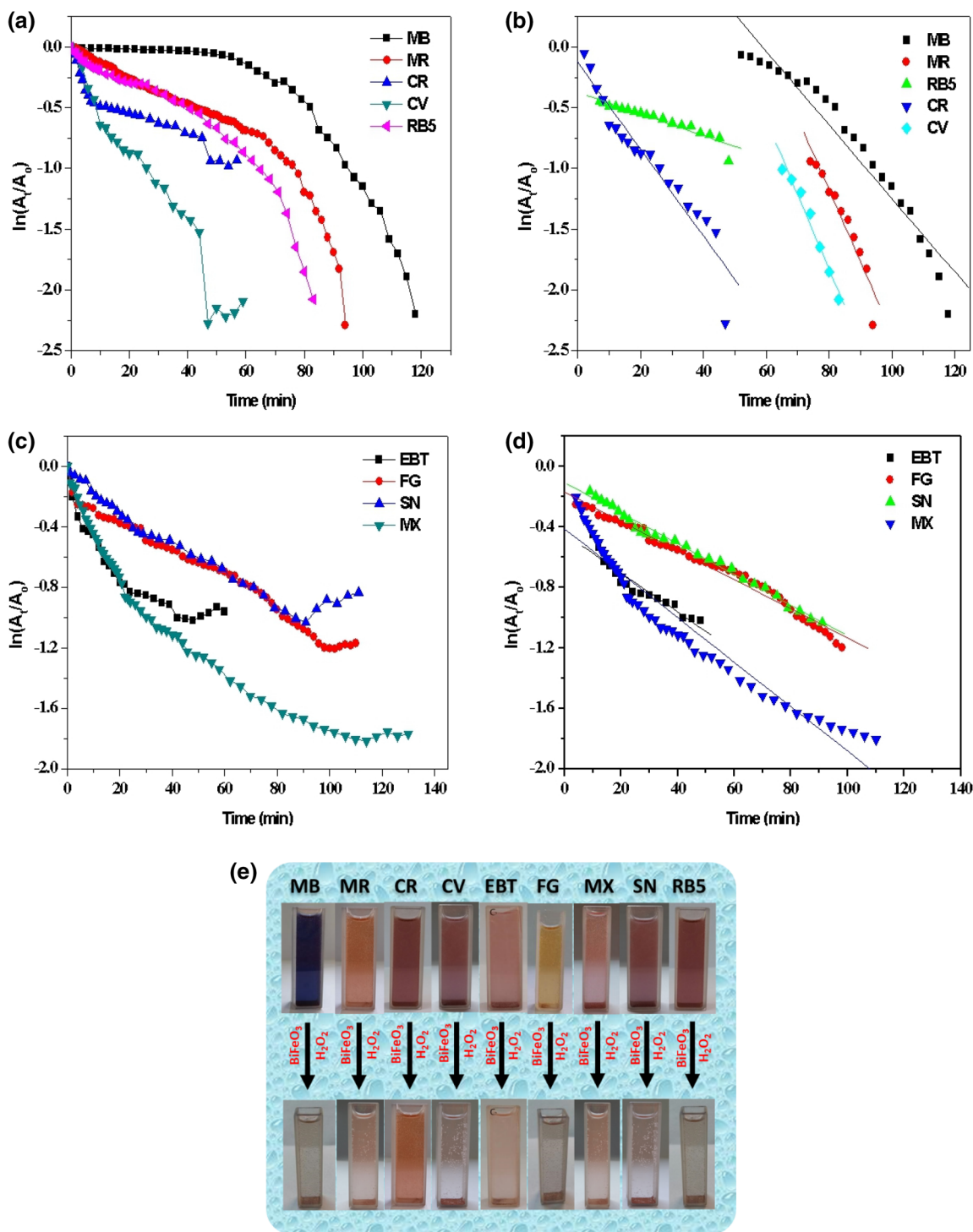


Fig. 4 a Plot of $\ln(A_t/A_0)$ versus time for degradation of MB, MR, CR, CV and RB5, and b determination of k_{app} . c Plot of $\ln(A_t/A_0)$ versus time for degradation of EBT, FG, SN and MX. d Plot of $\ln(A_t/A_0)$ versus time for determination of k_{app} . e Pictures of dyes before and after degradation

3.4.1 Comparison of Apparent Rate Constant of Degradation of Organic Dyes

Plot of comparison of k_{app} and substrate using BiFeO_3

$A_0)$ versus time for determination of k_{app} . e Pictures of dyes before and after degradation

bimetallic microparticles as catalyst at 25 °C temperature is shown in Fig. 5. Increasing order of k_{app} of organic dyes are $\text{CV} > \text{RB5} > \text{MR} > \text{MB} > \text{EBT} > \text{MX} > \text{CR} > \text{FG} > \text{SN}$ as shown in Fig. 5. The values of k_{app} are 0.0371,

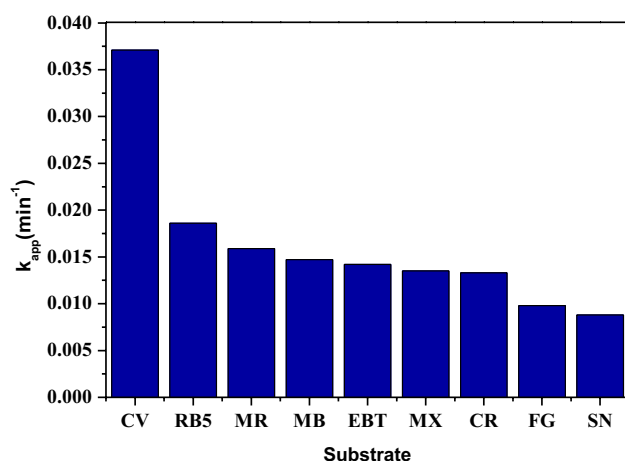


Fig. 5 Comparison of k_{app} values of degradation of different substrates using BiFeO_3 bimetallic microparticles catalyst

0.0186, 0.0159, 0.0147, 0.0142, 0.0135, 0.0133, 0.0098 and 0.0088 min^{-1} of organic dyes at 25°C temperature are CV, RB5, MR, MB, EBT, MX, CR, FG and SN respectively. k_{app} of CV is highest as compared to other organic dyes. BiFeO_3 microparticles as catalyst having binding sites and shows its highest ability for CV. Accessibility for CV is higher than other organic dyes due to binding affinity inside the microparticles. H_2O_2 easily degrade azo bond that present at periphery of the structure in CV. RB5 has k_{app} value smaller than that of CV because it has two degradation sites and hard to degrade because bulky groups present near unsaturated azo bonds. k_{app} of MR is greater than that of MB because not any bulky groups present near azo bond comparison to MB. The degradation of EBT is slow because azo bonds are attached between polycyclic aromatic rings. Azo bond is stuck between two rings that cause hindrance in degradation in MX. CR and FG also have two degradation sites because in CR azo bond present at para position and electrons are delocalized that produce difficulty in attacking, similarly in FG azo groups are attached with polycyclic aromatic compounds. Degradation of organic dyes also depend upon the bulkness of aromatic rings around azo group of dyes. SN restrict the cleavage of azo group due to resonance stability of its structure. Therefore, SN shows smallest k_{app} value among all substrates.

3.4.2 Comparison of Percentage Degradation of Organic Dyes

Plot of comparison of degradation of organic dyes in the presence of BiFeO_3 bimetallic microparticles as catalyst is shown in Fig. 6. Trend of percentage degradation of organic dyes is MR (90.28%) > MB (89.71%) > CV (89.14%) > RB5 (87.77%) > MX (83.42%) > FG (70.28%) > EBT

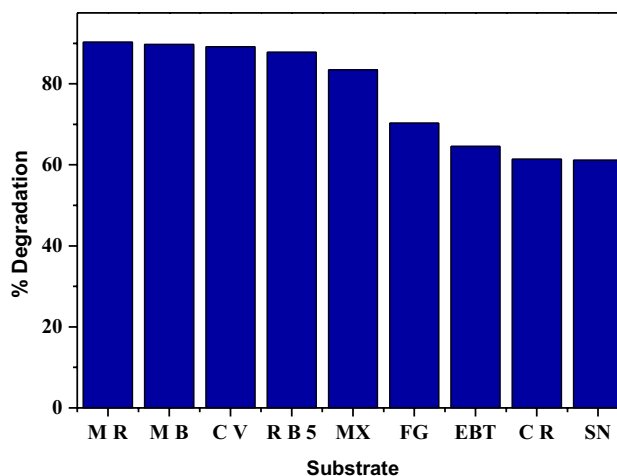


Fig. 6 Comparison of percentage degradation of organic dyes by using BiFeO_3 bimetallic microparticles as catalyst

(64.57%) > CR (61.37%) > SN (61.14%). Degradation of organic dyes depends upon the structure similarity, nature of bond breakage and orientation of functional group during the transfer of electron density. MR shows highest percentage degradation as compared to other organic dyes. Bulkness of the aromatic rings around azo group reduce the breaking of azo group by lowering its contact with catalyst and H_2O_2 and percentage degradation of organic dyes is decreased. Structures of all dyes are given in Fig. S3 to understand the connection between structure of dye and its degradation. SN shows lowest percentage degradation due to resonance stability of its structure because azo bond is connected with two benzenes. MR, MB, CV, RB5, MX and EBT, all possess exposed azo bond. Azo bond is present between two benzene rings or associated at a terminal. So its percentage degradation is high. Moreover due to long resonating systems, electrons of dye molecules do not develop strong coordination with catalyst surfaces, so these molecules easily desorb after degradation. So percentage degradation of these dyes is greater than that of CR and SN. CR and SN do not easily desorb after degradation. That's why their percentage degradation is low.

3.4.3 Comparison of Degradation Time of Organic Dyes

Figure 7 shows the plot between degradation time and organic dyes. Trend of degradation time of organic dyes is MB (118 min) > MX (114 min) > FG (102 min) > SN (95 min) > MR (94 min) > RB5 (83 min) > EBT (48 min) > CR (48 min) > CV (47 min). Degradation time of MB is higher as compared to other organic dyes. Adsorption of MB on the active site of BiFeO_3 bimetallic microparticles is low and it is responsible for the increment in degradation time. Bulkness of the aromatic rings

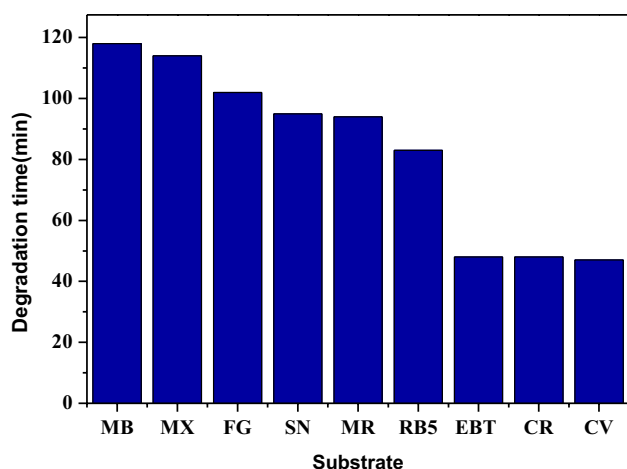


Fig. 7 Comparison of degradation time of various organic dyes by using BiFeO_3 bimetallic microparticles as catalyst

around the azo group is also responsible for the increase in degradation time. CV has lowest degradation time as shown in Fig. 7 due to the presence of less bulky aromatic rings around the azo group. These factors play role in increasing degradation time of MB as compared to CV. Degradation time of EBT, CR and CV are almost similar to each other. CR and EBT possess exposed azo bond which facilitates their degradation, so their degradation time is low. MX and MR possess carbonyl group which has high ability for adsorption on metal surfaces. So their degradation time is high and similar to MB. The chemical structures of all the dyes are given as Fig. S3.

4 Conclusions

BiFeO_3 microrods and microstars are synthesized by micro-emulsion method. XRD shows that product is highly crystalline and has trigonal (hexagonal axes) unit cell. Application of BiFeO_3 microparticles as catalyst and fuel additive are studied. It is concluded that vaporization and kinematic viscosity of fuel are increased by increasing additive dosage. High calorific value explained that addition of microparticles as additive is helpful in gaining heat energy. Therefore, BiFeO_3 microparticles increased the efficiency of fuel. BiFeO_3 microparticles are also used as catalyst for degradation of organic dyes. Degradation of dyes occurred very slowly with passage of time but the process was accelerated by addition of microparticles. MR shows highest percentage degradation and SN shows lowest percentage degradation due to the high stability of its structure. Degradation time of MB is highest and CV has lowest degradation time among all substrates studied.

Acknowledgements Authors are highly grateful to Department of Chemistry, University of Agriculture, Faisalabad 38000, Pakistan. Authors are also thankful to Community College, Post Agricultural Research Station, University of Agriculture, Faisalabad 38000, Pakistan

Compliance with Ethical Standards

Conflict of interest All the authors have declared no financial and non-financial interests.

References

1. R.W. Murray, *Chem. Rev.* **108**, 2688–2720 (2008)
2. Y. Bing, H. Liu, L. Zhang, D. Ghosh, J. Zhang, *Chem. Soc. Rev.* **39**, 2184–2202 (2010)
3. V.N. Nikiforov, E.Y. Filinova, *Mag. Nanopart.* **55**, 393–455 (2009)
4. S. Guo, E. Wang, *Acc. Chem. Res.* **44**, 491–500 (2011)
5. D.R. Kulkarni, S.J. Malode, K. Keerthi Prabhu, N.H. Ayachit, R.M. Kulkarni, N.P. Shetti, *Mater. Chem. Phys.* **246**, 122791 (2020)
6. J. Zhang, X. Qu, Y. Han, L. Shen, S. Yin, G. Li, Y. Jiang, S. Sun, *Appl B Catal* (2020). <https://doi.org/10.1016/j.apcatb.2019.118345>
7. X. Yuan, D. Dragoie, P. Beaunier, D.B. Uribe, L. Ramos, M.G. Méndez-Medrano, H. Remita, *J. Mater. Chem. A* **8**, 268–277 (2020)
8. N. Khalid, A. Majid, M.B. Tahir, N. Niaz, S. Khalid, *Ceram. Int.* **43**, 14552–14571 (2017)
9. M.B. Tahir, G. Nabi, T. Iqbal, M. Sagir, M. Rafique, *Ceram. Int.* **44**, 6686–6690 (2018)
10. M.B. Tahir, G. Nabi, N. Khalid, M. Rafique, *Ceram. Int.* **44**, 5705–5709 (2018)
11. N. Khalid, M. Liaqat, M.B. Tahir, G. Nabi, T. Iqbal, N. Niaz, *Ceram. Int.* **44**, 546–549 (2018)
12. W. Sun, X. Cai, Z. Wang, H. Zhao, M. Lana, *Microchem. J.* (2020). <https://doi.org/10.1016/j.microc.2020.104595>
13. M. Hyder, G.R.K. Reddy, B. Naveen, P.S. Kumar, *Chem Lett Phys* (2020). <https://doi.org/10.1016/j.cplett.2020.137086>
14. M. Yan, M. Zhang, S. Ge, J. Yu, M. Li, J. Huang, S. Liu, *Analyst* **137**, 3314–3320 (2012)
15. C.Y. Fu, K.W. Kho, U. Dinish, Z.Y. Koh, O. Malini, J. Raman Spect. **43**, 977–985 (2012)
16. C. Burda, X. Chen, R. Narayanan, M.A. El-Sayed, *Chem. Rev.* **105**, 1025–1102 (2005)
17. A.D. Bokare, R.C. Chikate, C.V. Rode, K.M. Paknikar, *Appl. Catal. B* **79**, 270–278 (2008)
18. F. Godínez-Salomón, R.N. Mendoza-Cruz, M.J. Arellano-Jimenez, M. Jose-Yacaman, C.P. Rhodes, *ACS Appl. Mater. Interface* **9**, 18660–18674 (2017)
19. A.U. Nilekar, S. Alayoglu, B. Eichhorn, M. Mavrikakis, *J. Am. Chem. Soc.* **132**, 7418–7428 (2010)
20. N. Khalid, E. Ahmed, N. Niaz, G. Nabi, M. Ahmad, M.B. Tahir, M. Rafique, M. Rizwan, Y. Khan, *Ceram. Int.* **43**, 6771–6777 (2017)
21. K. Deplanche, M.L. Merroun, M. Casadesus, D.T. Tran, I.P. Mikheenko, J.A. Bennett, J. Zhu, I.P. Jones, G.A. Attard, J. Wood, *J. R. Soc. Interface* **9**, 1705–1712 (2012)
22. C.H. Liu, R.H. Liu, Q.J. Sun, J.B. Chang, X. Gao, Y. Liu, S.T. Lee, Z.H. Kang, S.D. Wang, *Nanoscale* **7**, 6356–6362 (2015)
23. G. Fu, H. Liu, N. You, J. Wu, D. Sun, L. Xu, Y. Tang, Y. Chen, *Nano Res.* **9**, 755–765 (2016)

24. M. Hosseini, T. Barakat, R. Cousin, A. Aboukaïs, B.L. Su, G. De Weireld, S. Siffert, *Appl. Catal. B* **111**, 218–224 (2012)
25. Z. Han, S. Li, F. Jiang, T. Wang, X. Ma, J. Gong, *Nanoscale* **6**, 10000–10008 (2014)
26. W. Xie, C. Herrmann, K. Kömpe, M. Haase, S. Schlücker, *J. Am. Chem. Soc.* **133**, 19302–19305 (2011)
27. G.N. Jovanovic, P. ŽnidaršičPlazl, P. Sakrithichai, K. Al-Khaldi, *Ind. Eng. Chem. Res.* **44**, 5099–5106 (2005)
28. Z.-H. Lu, J. Li, A. Zhu, Q. Yao, W. Huang, R. Zhou, R. Zhou, X. Chen, *Int. J. Hydrogen Energy* **38**, 5330–5337 (2013)
29. H. Beygi, A. Babakhani, *J. Magn. Magn. Mater.* **421**, 177–183 (2017)
30. X. Nie, J. Liu, X. Zeng, D. Yue, *J. Environ. Sci.* **25**, 473–478 (2013)
31. N. Singh, K.J. Singh, K. Singh, H. Singh, *Nucl. Inst. Meth. Phys. Res.* **225**, 305–309 (2004)
32. S.H. Chen, C.C. Chen, Z. Luo, C.G. Chao, *Mater. Lett.* **63**, 1165–1168 (2009)
33. L. Zhang, Y. Zhu, *Catal. Sci. Technol.* **2**, 694–706 (2012)
34. Y.-H. Sung, S.-D. Huang, *Anal. Chim. Acta* **495**, 165–176 (2003)
35. H. Shokrollahi, *Powder Technol.* **235**, 953–958 (2013)
36. C. Chen, J. Cheng, S. Yu, L. Che, Z. Meng, *J. Cryst. Growth* **291**, 135–139 (2006)
37. I.H. Lone, A. Kalam, J. Ahmed, N. Alhokbany, S.M. Alshehri, T. Ahmad, *J. Nanosci. Nanotechnol.* **20**, 3823–3831 (2020)
38. S. Chakraborty, M. Pal, *J. Alloys Compd.* **787**, 1204–1211 (2019)
39. S. Ruby, D.R. Rosaline, S. Inbanathan, K. Anand, G. Kavitha, R. Srinivasan, A. Umar, H. Hegazy, H. Algarni, *J. Nanosci. Nanotechnol.* **20**, 1851–1858 (2020)
40. S.E. Musavi Ghahfarokhi, M.R. Larki, I. Kazeminezhad, *Vacuum* (2020). <https://doi.org/10.1016/j.vacuum.2019.109143>
41. C. Ponraj, G. Vinitha, J. Daniel, *Int. J. Green Energy* **17**, 71–83 (2020)
42. J. Cyriac, J.C. John, N. Kalarikkal, S. Augustine, *Mater Today* (2020). <https://doi.org/10.1016/j.matpr.2019.1012.1186>
43. A. Soam, R. Kumar, M. Singh, D. Thatoi, R.O. Dusane, *J. Alloys Compd.* **813**, 152145 (2020)
44. C.V. Reddy, I.N. Reddy, K. Ravindranadh, K.R. Reddy, N.P. Shetti, D. Kim, J. Shim, T.M. Aminabhavi, *J. Environ. Manag.* **260**, 110088 (2020)
45. C.V. Reddy, I.N. Reddy, V.V.N. Harish, K.R. Reddy, N.P. Shetti, J. Shim, T.M. Aminabhavi, *Chemosphere* **239**, 124766 (2020)
46. K.V. Karthik, C.V. Reddy, K.R. Reddy, R. Ravishankar, G. Sanjeev, R.V. Kulkarni, N.P. Shetti, A.V. Raghu, *J. Mater. Sci.* **30**, 20646–20653 (2019)
47. S. M., R. Ch Venkata, R.R. Kakarla, N.P. Shetti, R. M S, V.R. Anjanapura, *Mater. Res. Exp.* **6**, 125502–125504 (2019)
48. V. Navakoteswara Rao, N. Lakshmana Reddy, M. Mamatha Kumari, P. Ravi, M. Sathish, K.M. Kuruvilla, V. Preethi, K.R. Reddy, N.P. Shetti, T.M. Aminabhavi, M.V. Shankar, *Appl. Catal. B* **254**, 174–185 (2019)
49. K.R. Reddy, C.H.V. Reddy, M.N. Nadagouda, N.P. Shetti, S. Jaesool, T.M. Aminabhavi, *J. Environ. Manag.* **238**, 25–40 (2019)
50. A. Mishra, A. Mehta, S. Basu, N.P. Shetti, K.R. Reddy, T.M. Aminabhavi, *Carbon* **149**, 693–721 (2019)
51. Y. Wu, H. Wang, W. Tu, Y. Liu, Y.Z. Tan, X. Yuan, J.W. Chew, *J. Hazard. Mater.* **347**, 412–422 (2018)
52. S. Ahmed, M.G. Rasul, W.N. Martens, R. Brown, M.A. Hashib, *Water Air Soil Pollut.* **215**, 3–29 (2011)
53. A. AlNafey, A. Addad, B. Sieber, G. Chastanet, A. Barras, S. Szunerits, R. Boukherroub, *Chem. Eng. J.* **322**, 375–384 (2017)
54. N. Arora, A. Mehta, A. Mishra, S. Basu, *Appl. Clay Sci.* **151**, 1–9 (2018)
55. M. Cao, P. Wang, Y. Ao, C. Wang, J. Hou, J. Qian, *Chem. Eng. J.* **264**, 113–124 (2015)
56. V.N. Rao, N.L. Reddy, M.M. Kumari, K.K. Cheralathan, P. Ravi, M. Sathish, B. Neppolian, K.R. Reddy, N.P. Shetti, P. Prathap, T.M. Aminabhavi, M.V. Shankar, *J. Environ. Manag.* **248**, 109246 (2019)
57. N.L. Reddy, V.N. Rao, M. Vijayakumar, R. Santhosh, S. Anandan, M. Karthik, M.V. Shankar, K.R. Reddy, N.P. Shetti, M.N. Nadagouda, T.M. Aminabhavi, *Int. J. Hydrogen Energy* **44**, 10453–10472 (2019)
58. M.B. Tahir, G. Nabi, M. Rafique, N. Khalid, *Int. J. Environ. Sci. Technol.* **14**, 2519–2542 (2017)
59. M.U. Khalid, S.R. Khan, S. Jamil, *J. Inorg. Organomet. Polym. Mater.* **28**, 168–176 (2018)
60. S.R. Khan, M.U. Khalid, S. Jamil, S. Li, A. Mujahid, M.R.S.A. Janjua, *J. Water Health* **16**, 773–781 (2018)
61. S.R. Khan, S. Kanwal, M. Hashaam, S. Jamil, B. Ullah, M.R.S.A. Janjua, *Mater. Res. Exp.* **7**, 025036 (2020)
62. S.R. Khan, A. Naeem, S. Jamil, A.I. Aqib, M.R.S. Ashraf Janjua, *Environ Technol.* (2019). <https://doi.org/10.1080/09593330.09592019.01660414>
63. M.V. Kumar, A.V. Babu, P.R. Kumar, *Environ. Sci. Pollut. Res.* **26**, 7651–7664 (2019)
64. V. Sajith, C. Sobhan, G. Peterson, *Adv. Mech. Eng.* **2**, 581407–581417 (2010)
65. M. Tahir, G. Nabi, A. Hassan, T. Iqbal, H. Kiran, A. Majid, *J. Inorg. Organomet. Polym. Mater.* **28**, 738–745 (2018)
66. M.B. Tahir, M. Sagir, *Sep. Purif. Technol.* **209**, 94–102 (2019)
67. M.B. Tahir, G. Nabi, N. Khalid, *Mater. Sci. Semiconduc. Proc.* **84**, 36–41 (2018)
68. M.B. Tahir, *J. Inorg. Organomet. Polym. Mater.* **28**, 2160–2168 (2018)

Publisher's Note Springer Nature remains neutral with regard to jurisdictional claims in published maps and institutional affiliations.